

# Regional spectral characteristics, quality factor and site responses in western-central Sichuan, China (I): Application of parametric generalized inversion technique

Pengfei Dang<sup>a,b,\*</sup>, Jie Cui<sup>a</sup>, Hongfeng Yang<sup>b</sup>, Jian Song<sup>c</sup>

<sup>a</sup> School of Civil Engineering, Guangzhou University, No. 230 Waihuan West Road, Guangzhou, 510006, Guangdong Province, China

<sup>b</sup> Earth and Environmental Sciences Programme, Faculty of Science, The Chinese University of Hong Kong, Shatin, Hong Kong, 999077, China

<sup>c</sup> Guangdong Hualu Transportation Technology Co., Ltd, Guangdong Jiaoke Testing Co., Ltd, No. 1180 Guangcong Ba Road, Luotan Town, Baiyun District, 510550, Guangdong Province, Guangzhou, China

## ARTICLE INFO

### Keywords:

Western Sichuan  
Generalized inversion technique  
Source characteristics  
Quality factor  
Site effects

## ABSTRACT

To study the source, site amplification and seismic wave attenuation characteristics in the Sichuan area, 1242 ground motion recordings corresponding to 62 earthquake events with  $M_s$  4.3–6.4 recorded by 55 observation stations in the study area were selected. The source spectra, site effects and frequency-related quality factors in the western Sichuan area were inverted by the generalized inversion technique. Then, the source parameters, such as corner frequency, seismic moment and stress drop, were estimated by a grid-searching tool. In the generalized inversion method, a bedrock station was used to remove the trade-off between the site and source components. The inverted quality factor of 0.25–20 Hz frequency band is characterized as  $Q(f) = 219.4f^{0.7383}$ . The results indicate that the inverted source spectrum is well matched with the  $\omega^2$  source model, in which the stress parameter values range between 0.2 MPa and 3.5 MPa, with an average value of 1.2 MPa and source radii between 0.3 and 4 km. In addition, a comparison between the inversion results obtained from the horizontal-to-vertical spectral ratio and the generalized inversion methods indicates that these two approaches actually describe the same level of site effect, while the averaged site effect obtained by the generalized inversion method is always greater than the result obtained by the horizontal-to-vertical spectral ratio method. Finally, a residual defined as a function of hypocentral distance and moment magnitude was used to investigate whether there was any bias in the inversion results. The results indicate that the geometric spreading and source model used in this study resulted in an underestimation of the Fourier amplitude level in the far field and for large earthquakes. The results of this study can be applied in ground motion simulation and prediction to help the study of seismic disasters and risk assessment in the study area.

## 1. Introduction

The physical and mechanical properties and stress state dynamic changes of crustal media in post-earthquake areas are particularly important for studying and predicting the development trend of earthquake sequences. The use of seismic waves to study the attenuation characteristics of media, internal structural characteristics of the crust, and strong ground motion characteristics has become an important research topic in the field of seismic engineering. In the study of site response at different stations, Cultrera et al. [1] incorporated seismic recordings into the horizontal-to-vertical spectral ratio (H/V) method and found that the site amplification results obtained from H/V showed

significant variability, but the corner frequency was mainly in the 1–5 Hz frequency band. The application of H/V assumes that the vertical component of seismic waves remains basically unchanged during the propagation process. However, due to the complexity of the transmission medium of seismic waves, the vertical component of seismic waves can be affected by various factors, such as soft soil and terrain, making the application conditions of the H/V method extremely harsh, and there are significant limitations in estimating site amplification.

The parametric generalized inversion technique (GIT) proposed by Andrews [2] decomposes strong motion recordings into three sets of characteristic parameters: source, site and path. It has been widely used in the field of seismic engineering to evaluate the site effect [3–10].

\* Corresponding author. School of Civil Engineering, Guangzhou University, No. 230 Waihuan West Road, Guangzhou, 510006, Guangdong Province, China.  
E-mail addresses: [iempengfeid@gzhu.edu.cn](mailto:iempengfeid@gzhu.edu.cn) (P. Dang), [jcui@gzhu.edu.cn](mailto:jcui@gzhu.edu.cn) (J. Cui), [hyang@cuhk.edu.hk](mailto:hyang@cuhk.edu.hk) (H. Yang), [913606737@qq.com](mailto:913606737@qq.com) (J. Song).

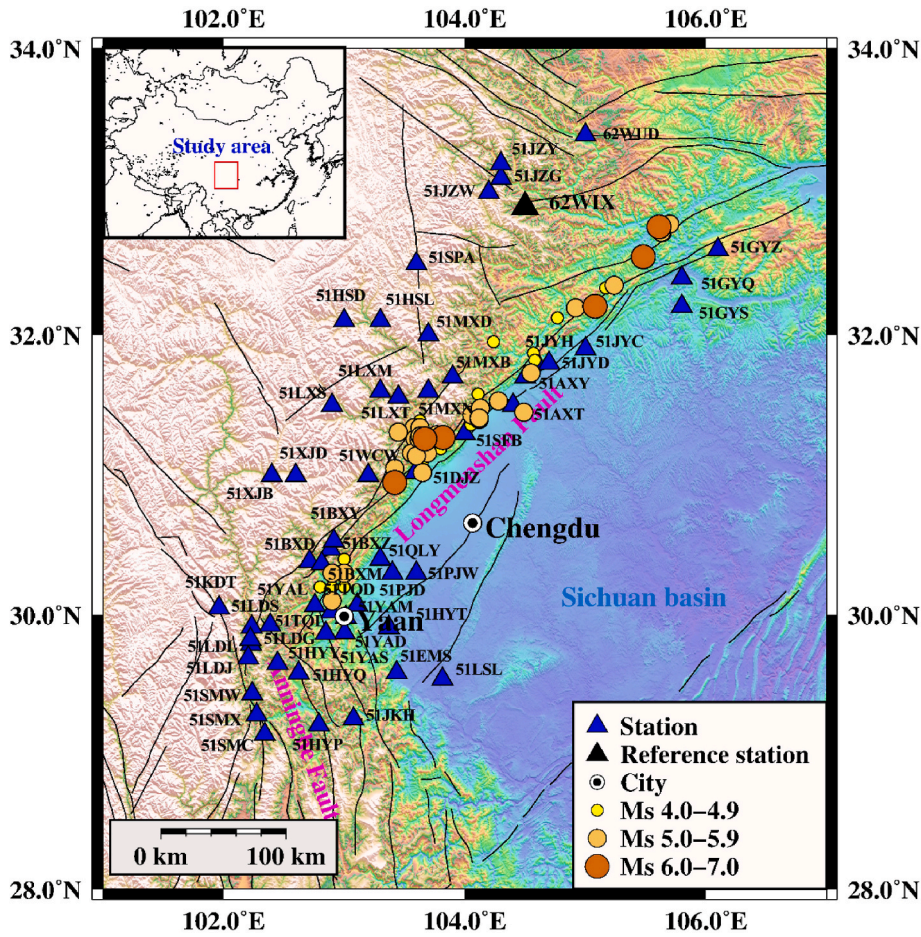


Fig. 1. The distributions of earthquake events (circles) and stations (triangles) selected in this study. Thin solid lines represent faults, and blue and black triangles represent strong motion stations and reference station, respectively. Inset map shows the location of the study area.

In our scheme, the Fourier amplitude spectrum (FAS) of the shear-wave is adopted to calculate the earthquake source, site response and path attenuation. Considering the earthquake events that occurred during a long period from 2008 to 2022, almost all major earthquake

events in the area have been analyzed. These earthquake events were recorded at different strong-motion stations, which are located in a large area of the western Sichuan area and cover a wide range of hypocentral distances. Therefore, more general path attenuation parameters can be

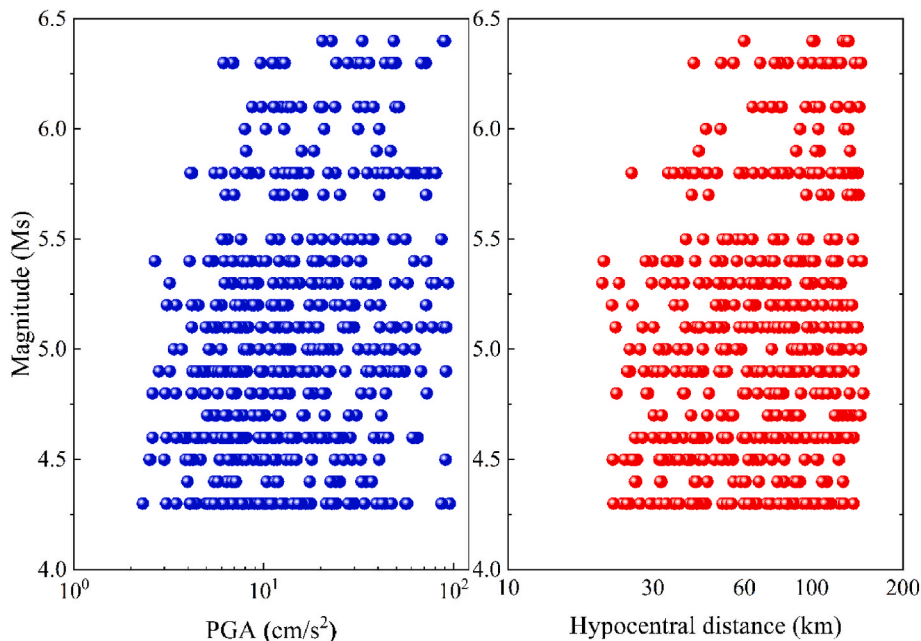


Fig. 2. The relationship between magnitude and peak ground acceleration (left panel) and hypocentral distance (right panel).

**Table 1**

The name, geographic coordinates, site condition and number of recordings of selected stations.

No.	Station code	Latitude (°)	Longitude (°)	Number of records	Site condition
1	51PJW	30.3	103.6	22	Soil
2	51WCW	31.0	103.2	24	Soil
3	51MXN	31.6	103.7	54	Soil
4	51MXD	32.0	103.7	74	Soil
5	51XJD	31.0	102.6	14	Soil
6	51SPA	32.5	103.6	24	Soil
7	51MXB	31.7	103.9	12	Soil
8	51XJB	31.0	102.4	16	Soil
9	51HSL	32.1	103.3	26	Soil
10	51LXS	31.5	102.9	38	Soil
11	51JYH	31.8	104.6	36	Soil
12	51AXT	31.5	104.4	12	Soil
13	51JYC	31.9	105.0	36	Soil
14	51HSD	32.1	103.0	26	Soil
15	51JYD	31.8	104.7	20	Soil
16	51AXY	31.7	104.5	32	Soil
17	51PJD	30.3	103.4	32	Soil
18	51QLY	30.4	103.3	20	Soil
19	51LXM	31.6	103.3	54	Soil
20	51BXZ	30.4	102.9	12	Rock
21	51EMS	29.6	103.4	14	Soil
22	51LSL	29.5	103.8	14	Soil
23	51BXM	30.4	102.7	30	Soil
24	51YAD	29.9	103.0	30	Soil
25	51HYT	29.9	103.4	20	Soil
26	51YAM	30.1	103.1	24	Soil
27	51TQL	29.9	102.4	24	Soil
28	51BXY	30.5	102.9	26	Soil
29	51DJZ	31.0	103.5	18	Soil
30	51YAS	29.8	103.0	28	Soil
31	51KDT	30.0	101.9	12	Soil
32	51LDL	29.7	102.2	22	Soil
33	51LDS	29.9	102.2	16	Soil
34	51SMW	29.4	102.2	22	Soil
35	51HYY	29.6	102.4	22	Soil
36	51YAL	29.8	102.8	22	Soil
37	51LDL	29.6	102.2	22	Soil
38	51HYP	29.2	102.8	14	Soil
39	51HYQ	29.6	102.6	16	Soil
40	51SMX	29.2	102.2	14	Soil
41	51TQD	30.1	102.7	20	Soil
42	51JKH	29.2	103.1	10	Soil
43	51LXT	31.5	103.4	48	Soil
44	51BXD	30.4	102.8	20	Rock
45	51LDG	29.8	102.2	12	Soil
46	51LSF	30.0	102.9	12	Soil
47	51SMC	29.1	102.3	10	Soil
48	51SFB	31.3	104.0	8	Soil
49	51GYS	32.2	105.8	8	Soil
50	62WUD	33.4	105.0	20	Soil
51	51GYZ	32.6	106.1	12	Soil
52	51JZW	33.0	104.2	12	Soil
53	51JZG	33.1	104.3	16	Soil
54	51JZY	33.2	104.3	16	Soil
55	<b>62WIX</b>	32.9	104.5	14	Rock
56	51GYQ	32.4	105.8	10	Soil

**Note:** The site conditions are as indicated in the headlines of raw acceleration files. The bold character indicates the selected reference station.

estimated from the selected earthquake recordings. Although site effects in the Sichuan region have been studied by many scholars [10–12], this study attempts to study region-specific earthquake parameters for the western Sichuan, China. In addition, we try to systematically determined the earthquake source parameters, shear-wave attenuation characteristics and site effects from strong motion recordings in the study region. Then, the results are compared with the inversion results given by previous studies for different regions.

## 2. Dataset

This study collected strong-motion recordings in the Sichuan region from 2008 to 2022, based on the following principles:

- (1) The hypocentral distance is between 20 km and 150 km. The data distribution within the hypocentral distance range is relatively dense, which can reduce the degree of dispersion and increase the stability of the inversion results. The range of hypocentral distance basically satisfies the assumption that geometric diffusion is the derivative of hypocentral distance [13,14].
- (2) The average peak ground accelerations (PGAs) in both horizontal components range from 2 cm/s<sup>2</sup> to 100 cm/s<sup>2</sup>. This not only reduces the impact of background noise on the site, but also avoids the nonlinear response of the soil layer on the site.
- (3) An earthquake event is recorded by at least four strong-motion stations, and each station is triggered by at least four earthquakes to reduce data discreteness and ensure inversion algorithm stability.

Therefore, a total of 55 stations and 1242 horizontal records of 62 earthquakes were selected. It should be noted that the earthquake events we selected in this study are completely different from those used by Wang et al. [15], although some of the earthquake events were from the 2008 Wenchuan aftershocks. In this study, the 2013 Lushan aftershocks were also selected. Fig. 1 shows the distribution positions of stations and earthquake sources, with station 62WIX selected as the bedrock station, represented by a black triangle in the figure. Fig. 2 shows the relationship between the magnitude of ground motion records and hypocentral distance and PGA. In addition, the station code, general location, site condition and number of recordings are given in Table 1.

## 3. Data processing

The selected earthquake recordings were filtered between 0.25 and 20 Hz using a fourth-order Butterworth filter after baseline correcting for their individual baseline effects. The shear-wave amplitude spectra of the horizontal components were then obtained based on the method provided by Husid [16] and McCann [17]. The onset of the P- and shear-waves were defined as the abruptly increased point in the Husid curves, and the offset of the shear-wave was determined by the energy approach given by Pacor et al. [18]. The Husid plot is a graphical approach used in seismology to determine the S waves arrival times, however, it has some limitations. (1) Lack of clear separation. The separation between P and S wave on the plot is not always well-defined, especially in the presence of noise or complex waveforms. (2) Incomplete waveforms. The S wave often have lower amplitudes compared to P waves, and they can get easily masked by noise or other arrivals. In cases where the S-wave arrival is weak or poorly recorded. (3) Complex waveforms. The Husid plot assumes a simple waveform with distinct arrivals, but in reality, the waveform can be more complicated. (4) Velocity heterogeneities. The velocity of seismic waves can vary due to heterogeneities in the Earth's structure, which make it difficult to accurately determine S-wave arrival times. (5) Geometrical spreading. The geometrical spreading can affect the identification of S-wave arrivals on the Husid plot, especially when the S-wave amplitudes are already low. The end of the noise window was determined to be 2.0 s before the beginning of the P-wave. A 10 % Hanning taper was used at both ends of the shear-wave window to eliminate truncation errors [7]. The FAS of the shear- and P-waves with the same length were obtained and smoothed by the windowing function defined by Konno and Ohmachi [19] with parameter  $b$  equal to 20. In this study, the root-mean-square of the two horizontal FAS values was calculated to

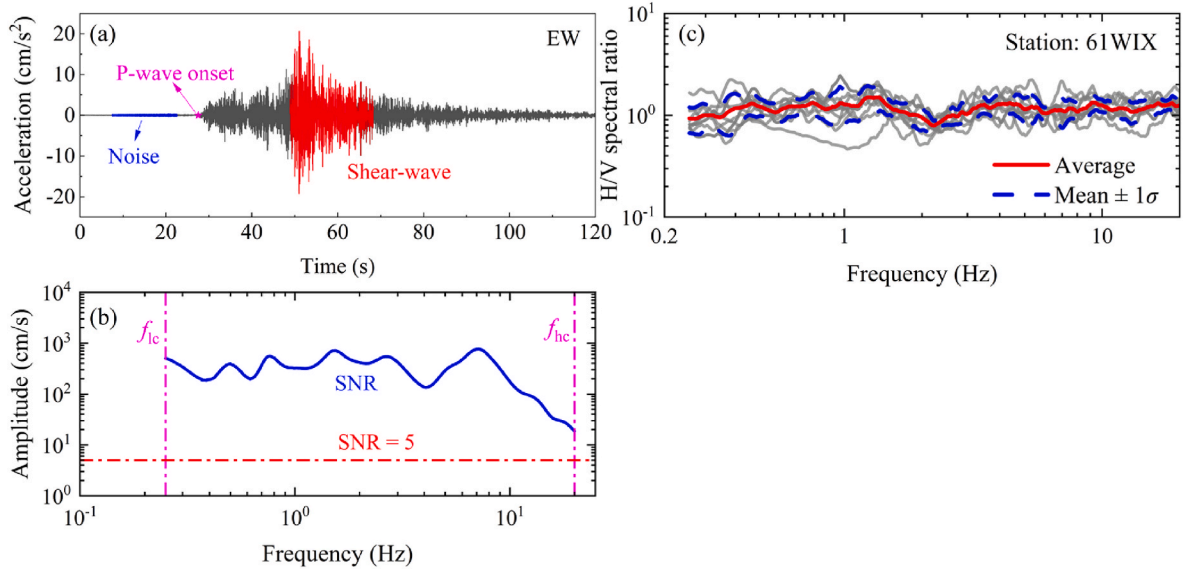


**Fig. 3.** (A) An example of extracting the shear-wave and P-wave. The red and blue sections indicate the shear-wave and P-wave, respectively; the magenta pentagram represents the onset of the P-wave. (b) SNR (blue solid line) obtained in this study. (c) H/V spectral ratio at station 61WIX. The red line indicates the average value, and the blue dotted lines represent the range of the average plus or minus one standard deviation.

define the horizontal amplitude of earthquake ground motion of the shear-wave in the frequency domain. Fig. 3a indicates the extracted shear- and P-waves. In our scheme, a signal-to-noise ratio (SNR) threshold of 5 was used (Fig. 3b). The high-cut corner frequency  $f_{hc}$  was determined to be 20 Hz, and the low-cut corner frequency  $f_{lc}$  was defined by the SNR [9] and was set to 0.25 Hz. Fig. 3c indicates the spectral ratio at station 61WIX, indicating that the site effects are nearly constrained to be 1.0 around all frequencies.

#### 4. Methodology

The seismic waves generated by the earthquake source will undergo multiple reflections, refractions, and transmissions during their propagation in the crustal medium. The seismic waves will decay with the dissipation of energy, but in the shallow medium above the earth, they will be amplified due to a decrease in wave impedance.

The GIT proposed by Andrews [2] represents ground motion observed on the surface as the convolution of three factors: source, path, and site in the time domain, effectively separating the three parameters of ground motion:

$$O_{ij}(f) = S_i(f)G_j(f)P_{ij}(f, R_{ij}) \quad (1)$$

in which  $O_{ij}(f)$  denotes the FAS of the shear-wave horizontal acceleration observed by the  $i$ th earthquake recordings at the  $j$ th station.  $S_i(f)$ ,  $G_j(f)$  and  $P_{ij}(f, R_{ij})$  denote the source term, site term and path term, respectively.  $R_{ij}$  represents the distance from the  $i$ th earthquake event to the  $j$ th station (km).

The path term  $P_{ij}(f, R_{ij})$  can be defined as the geometric spreading function  $GS(R_{ij})$  and anelastic attenuation:

$$P_{ij}(f) = GS(R_{ij}) \exp(-\pi f R_{ij} / [Q(f)\beta]) \quad (2)$$

where  $Q(f)$  represents the quality factor, and  $\beta$  denotes the shear-wave velocity and is set as 3.6 km/s for the Sichuan area [15,20,21].

In this study, the geometric spreading function  $GS(R_{ij})$  can be represented by the three linear decay curves given by Atkinson and Mereu [22] as follows:

$$GS(R) = \begin{cases} R^{-b_1} & R \leq R_{01} \\ R_{01}^{-b_1} R_{02}^{-b_2} R^{-b_2} & R_{01} < R \leq R_{02} \\ R_{01}^{-b_1} R_{02}^{-b_2} R^{-b_2} & R > R_{02} \end{cases} \quad (3)$$

where  $b_1 = 1.0$ ,  $b_2 = 0.5$ ,  $R_{01} = 1.5D$ , and  $R_{02} = 2.5D$ , in which  $D$  indicates the Moho depth. The average depth of the Moho surface in central Sichuan is approximately 47 km [23]. Therefore,  $R_{01}$  and  $R_{02}$  in the adopted geometrical spreading were defined as  $R_{01} = 70.5$  km and  $R_{02} = 117.5$  km, respectively. This model has usually been adopted in previous studies to describe the propagation of shear waves in the crust [10,24,25]. However, we simply adopted the  $R^{-1}$  attenuation model for the selected distance in this study [9,15].

The site effect  $G_j(f)$  describing site amplification and the diminution function was defined as follows [26]:

$$G_i(f) = A_i(f) \exp(-\pi f \kappa_0) \quad (4)$$

in which  $A_j(f)$  denotes the average site amplification factors obtained from the quarter-wavelength approximation method, and  $\kappa_0$  denotes the attenuation factor of the near-surface geological structures [27].

Substituting Equations (2) and (3) into Equation (1) and executing a logarithmic transformation on both sides of Equation (1) yields the following result:

$$\ln O_{ij}(f) - \ln GS(R_{ij}) = \ln S_i(f) + \ln G_j(f) - \pi f R_{ij} / [Q(f)\beta] \quad (5)$$

If the total number of data  $N$  corresponds to the number of events  $i$  recorded at the total number of stations  $j$ , then Equation (5) can be written in the following compact matrix:

$$\begin{bmatrix} 1 & 0 & 0 & \dots & 1 & 0 & 0 & \dots & -\pi f R_{11}/V \\ 1 & 0 & 0 & \dots & 0 & 1 & 0 & \dots & -\pi f R_{12}/V \\ \vdots & \vdots \\ 0 & 1 & 0 & \dots & 1 & 0 & 0 & \dots & -\pi f R_{21}/V \\ 0 & 1 & 0 & \dots & 0 & 1 & 0 & \dots & -\pi f R_{22}/V \\ \vdots & \vdots \\ 0 & 0 & \dots & 1 & 0 & 0 & \dots & 1 & -\pi f R_{ij}/V \end{bmatrix} \begin{bmatrix} \ln S_1(f) \\ \ln S_2(f) \\ \vdots \\ \ln S_i(f) \\ \ln G_1(f) \\ \ln G_2(f) \\ \vdots \\ \ln G_j(f) \\ 1/Q(f) \end{bmatrix} = \begin{bmatrix} \ln Q_{11}(f) - \ln GS(R_{11}) \\ \ln Q_{12}(f) - \ln GS(R_{12}) \\ \vdots \\ \ln Q_{21}(f) - \ln GS(R_{21}) \\ \ln Q_{22}(f) - \ln GS(R_{22}) \\ \vdots \\ \ln Q_{ij}(f) - \ln GS(R_{ij}) \end{bmatrix} \quad (6)$$

or

$$Ax = b \quad (7)$$

where  $A$  denotes the sparse matrix with only three nonzero elements in each row.  $b$  denotes a vector containing two elements of seismic Fourier amplitude and geometrical attenuation.  $x$  denotes the matrix that has  $i + j + 1$  unknown terms, such as quality factor  $Q(f)$ , source spectra  $\ln S_i(f)$  and site effects  $\ln G_j(f)$ ; each of its numbers denotes that this vector has  $n$  rows of elements.

Andrews [2] first reported the existence of an undetermined degree of freedom in Equation (7). This uncertain degree of freedom can be removed by selecting a reference site where the site effect can be regarded as an approximately constant value. Then the vector containing unknown source, path and site components can be obtained by the singular value decomposition algorithm proposed by Menke [28]:

$$x = (A^T A)^{-1} A^T b \quad (8)$$

### 5. Results and analysis

The source spectra of 62 earthquake events, site responses for 55 stations and path attenuation can be estimated by using the GIT to the selected earthquake recordings.

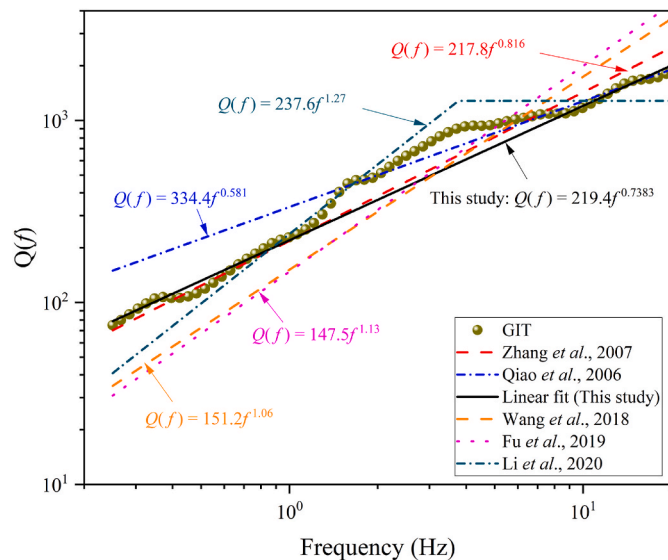


**Fig. 4.** The quality factors inverted in this study and previous studies. The balls indicate the inversion results using the GIT method. The black solid line indicates the best fitted model  $Q(f) = 219.4f^{0.7383}$ , and the blue dashed-dotted and red lines represent the inverted model  $Q(f) = 334.4f^{0.581}$  given by Qiao et al. [31] for the northwest Sichuan area and  $Q(f) = 217.8f^{0.816}$  given by Zhang et al. [30] for the Sichuan Basin area, respectively. Orange dashed, magenta dotted, and dark green dotted lines represent the quality factor models given by Wang et al. [15], Fu et al. [24] and Li et al. [25], respectively.

#### 5.1. High-frequency spectral decay

In GIT method, the high-frequency spectral decay parameter kappa ( $\kappa_0$ ) plays a critical role when determining the local site conditions. The zero-distance  $\kappa_0$  can be obtained from best-fitted line, which can be written in the form of  $\kappa = \kappa_0 + mR$ , in which  $R$  indicates the fault distance or epicentral distance in km. In this study, the regional kappa value of 0.033 s was adopted [21], which was slightly larger than the average kappa value of 0.0319 s for the mountain areas in Sichuan and greater than the average kappa value of 0.0475 s estimated for the Sichuan basin area [10]. This reason may be due to the surficial soil layers where the stations are located [24,29].

#### 5.2. Anelastic attenuation

The quality factor  $Q(f)$  is an important factor for characterizing the attenuation characteristics of earthquake ground motion. A larger  $Q(f)$  indicates slower attenuation of the ground motion. Generally, the quality factor of deep crustal media is larger, and the inelastic attenuation is weaker. When the observation station is far from the source, seismic rays mainly propagate along the Moho surface [22]; when the station is close to the source, seismic rays mainly propagate along the upper crust, with a critical distance of approximately 2.5 times the thickness of the crust [22]. In this study, the shear-wave quality factor within 150 km of the hypocentral distance is calculated by the GIT method, and it is fitted by the least square method and can be defined as  $Q(f) = 219.4f^{0.7382}$ . From the fitting results, the attenuation of seismic waves in the near-field area of western Sichuan is characterized by slow absorption with high  $Q_0$  and small  $\eta$  values. Fig. 4 plots the calculated frequency-related quality factors and their fitting results and compares the calculation results of this study with the simulation results given by Zhang et al. [30] for the Sichuan Basin region, Qiao et al. [31] for the northwest Sichuan region, Wang et al. [15] for Wenchuan aftershocks and Fu et al. [24] for the Sichuan Basin region, respectively. It can be seen in the figure that the 0.25–1.5 Hz quality factor fitting results of this study almost coincide with the simulation results of the model  $Q(f) = 217.8f^{0.816}$  given by Zhang et al. [30] for the Sichuan Basin region. However, the fitting results are very similar to the model  $Q(f) = 334.4f^{0.581}$  given by Qiao et al. [31] in the 10–20 Hz frequency band but smaller than those models of Zhang et al. [30] and Qiao et al. [31] in other frequency bands. Moreover, our fitting results are greater than the results of Wang et al. [15] and Fu et al. [24] in the frequency range less than 3 Hz, while in the frequency range greater than 3 Hz, they are less than the results given by Wang et al. [15] and Fu et al. [24]. However, the result given by Li et al. [25] for Changning earthquake are quite different from others, especially in the high frequencies ( $f > 4$  Hz). The source depth selected in this study is mainly 7–30 km, and the hypocentral distance is concentrated in the range of 20–150 km. The average depth of the crust in this study area is approximately 47 km [23]. The propagation path of seismic waves is mainly concentrated in the upper crust, and the quality factor of the deep crust medium is always larger [32]. Compared with the ground motion recordings selected by Zhang et al. [30] and Qiao et al. [31], the hypocentral distance in this study is

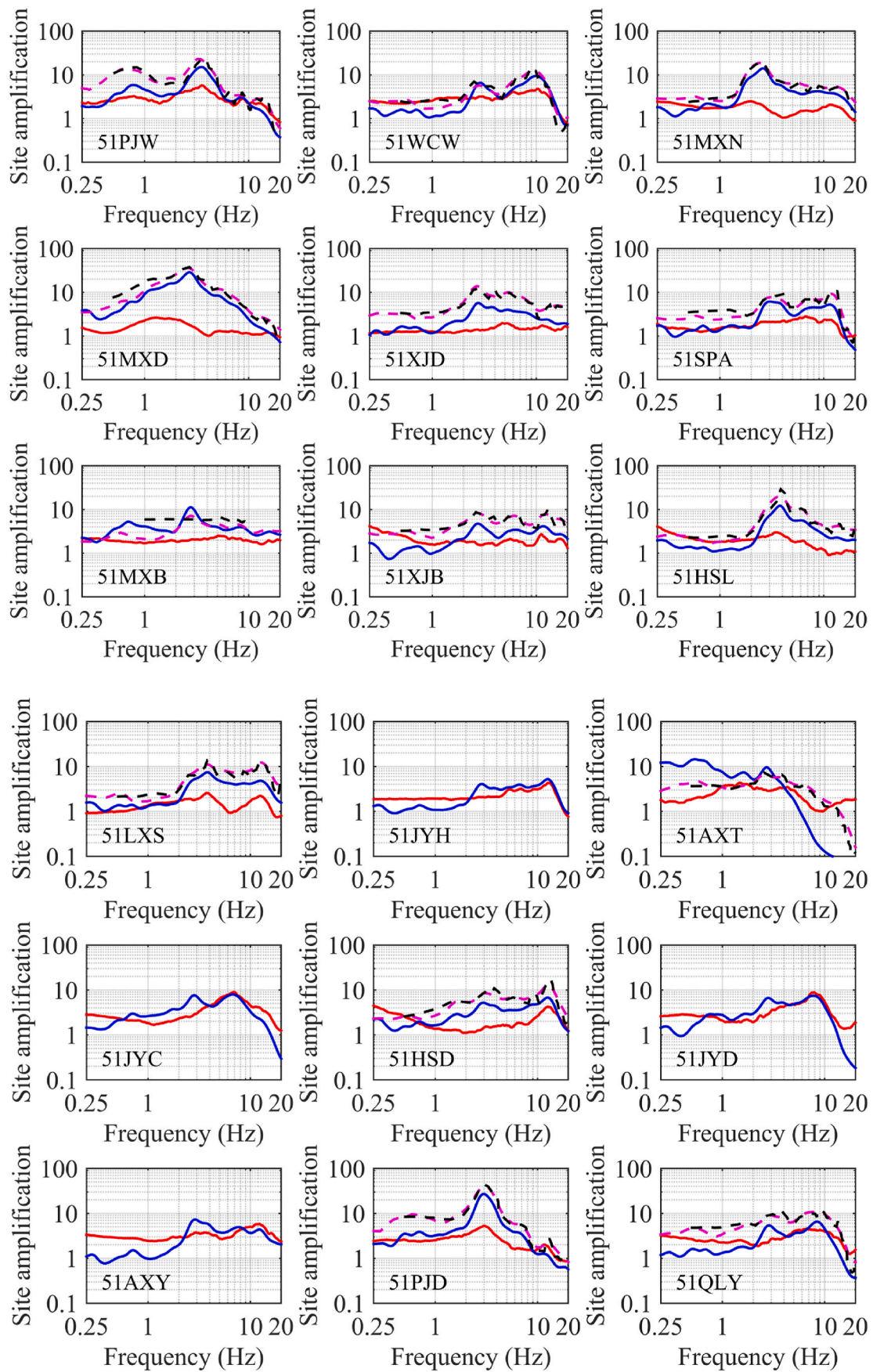


Fig. 5. Site effect at 55 selected stations calculated by the GIT (blue) and H/V (red) methods. The red solid line indicates the average value obtained from H/V spectral ratio method. The magenta and black dashed lines represent the inversion results of Wang et al. [15] and Ren et al. [11], respectively.

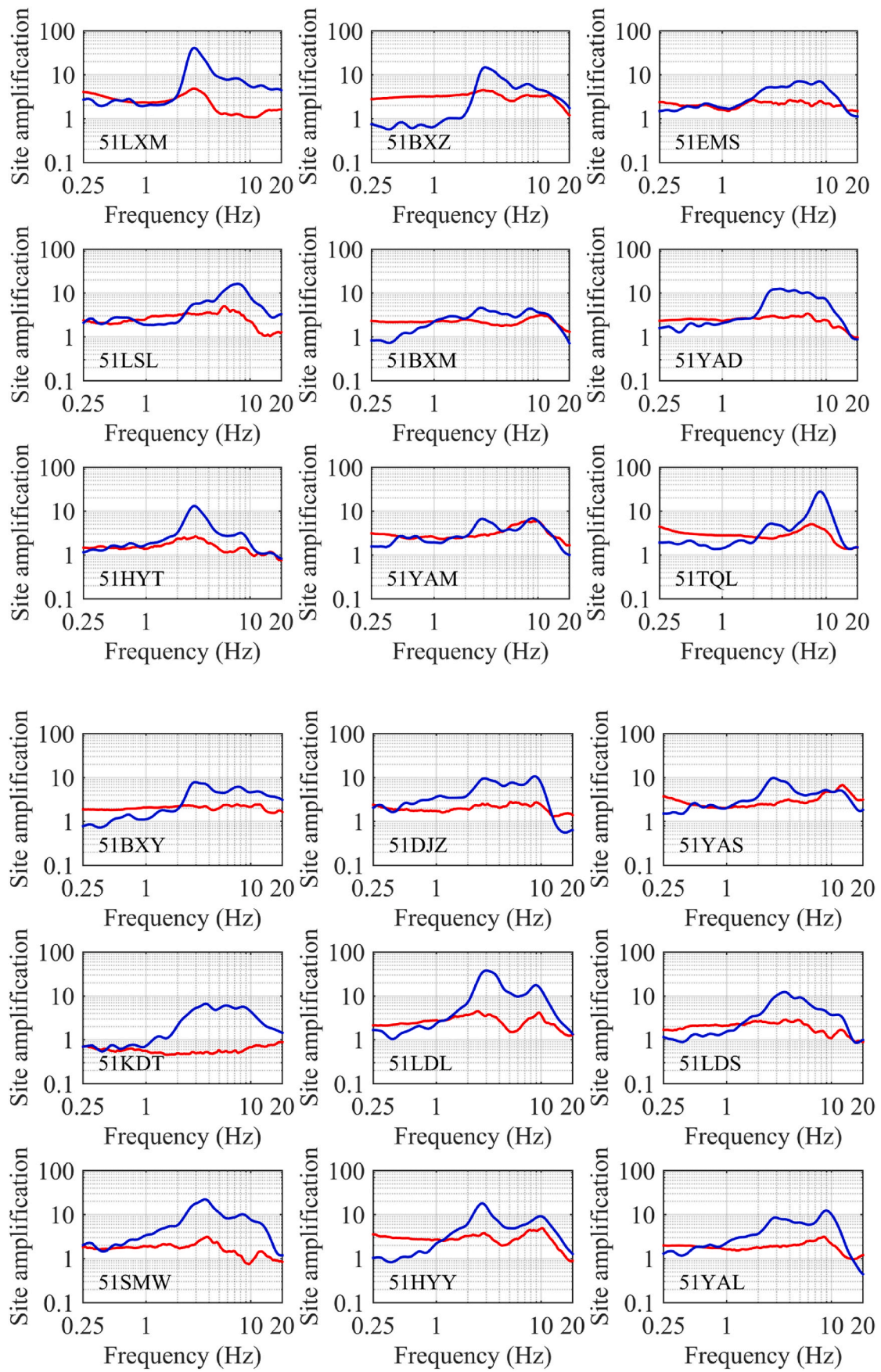


Fig. 5. (continued).

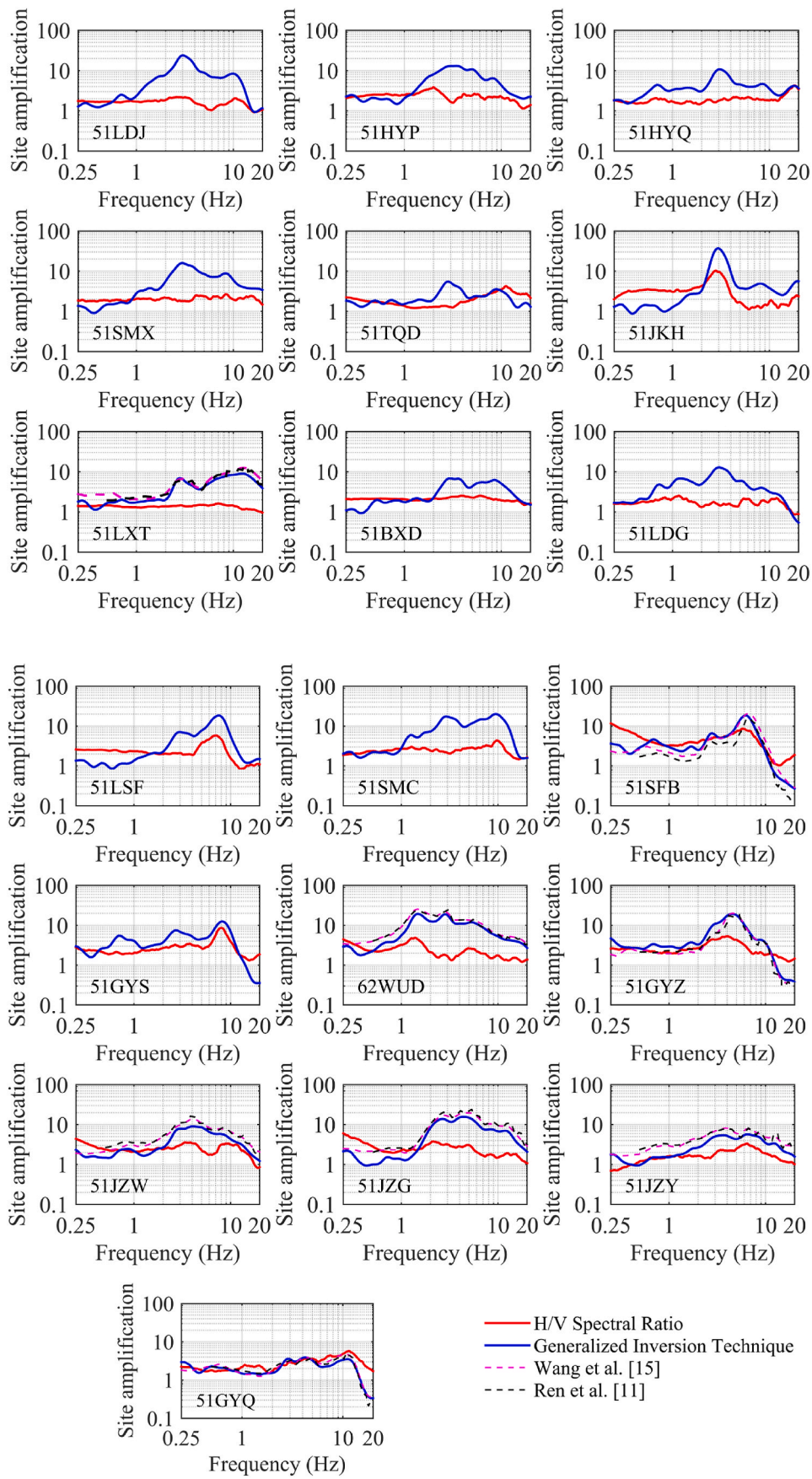
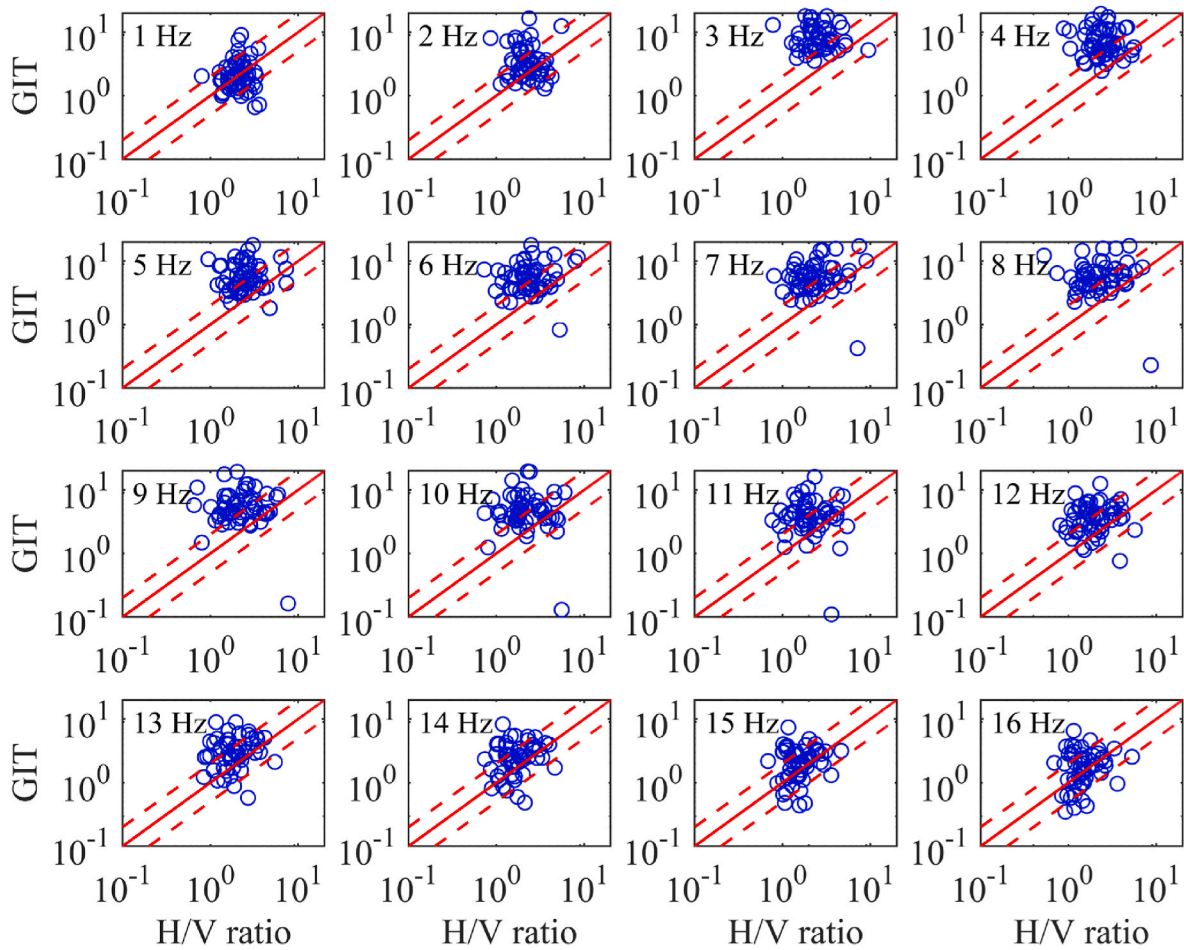


Fig. 5. (continued).



**Fig. 6.** Comparison of the site effect between the results obtained from the GIT and H/V methods at 16 selected frequency points. The circles indicate the site effect averaged over all stations. The dashed and solid lines indicate the 1:2, 2:1, and 1:1 correspondence.

smaller, and the quality factor is relatively small. At the same time, due to the concentration of the earthquake-prone area of Sichuan in this study, there is strong crustal activity in this area. It is generally believed that the  $Q$  value is relatively high in areas with relatively stable crustal activity and relatively small in areas with strong crustal activity [33]. In addition, different datasets and propagation paths will cause significant differences in quality factor [24].

### 5.3. Site responses

The H/V spectral ratio approach proposed by Lermo and Chavez-Garcia [34] has been applied by many scholars for different regions. This method assumes that there is no significant change in the vertical component of seismic waves during their propagation in the medium. By calculating the ratio of the horizontal and vertical components of seismic waves, the site amplification in the study region can be obtained. However, due to the mutual conversion of shear waves and P waves in soft soil strata [35], the two-dimensional and three-dimensional effects of sedimentary basin edges and terrain, and the inability to completely separate shear waves and P waves, the site amplification amplitude calculated by using the H/V spectral ratio has difficulty reflecting the real site amplification in this area, while the H/V ratios can reveal the predominant frequency peaks [36–39].

The GIT and H/V methods were adopted to obtain the site amplification at 55 stations, as shown in Fig. 5. The site responses for most selected strong-motion stations are quite consistent with those inverted by Wang et al. [15] and Ren et al. [11]. The comparison between the inverted results obtained by the H/V and GIT approaches indicates that

these two adopted approaches actually describe the same predominant frequency peaks; however, the general conclusion is that the H/V spectral ratio method fails in amplitude level, especially for higher modes [7,40]. In this study, the averaged site effects obtained by the generalized inversion method are significantly greater than the results obtained by the H/V spectral ratio method in the high frequencies with  $f$  greater than 2 Hz, while lower than the results obtained by H/V method in the high frequencies with  $f$  lower than 2 Hz. Overall, our inversion results are in good agreement with the results of Wang et al. [15]. In fact, the H/V spectral ratio approach can roughly estimate the predominant frequency of site, while underestimates the site amplification [15, 41–44].

The site effects obtained from the GIT and H/V approaches were averaged at several frequency points ranging from 1 to 16 Hz with an interval of 1 Hz, which is shown in Fig. 6. The comparison between the results obtained by the GIT and H/V approaches indicates that in the frequency range of 2–12 Hz, the GIT results are greater than the H/V results, while in the frequency range below 2 Hz and above 12 Hz, the GIT results are smaller than the H/V results, which is in agreement with the results given by Wang et al. [15]. The same conclusion can also be found in Fig. 5.

### 5.4. Spectral characteristics

In this study, a bootstrap analysis method given by Oth et al. [45] was adopted to investigate the stability of the inverted results. Some of the records were randomly removed from the datasets, and the remaining seismic records were considered as new datasets. Finally, 50

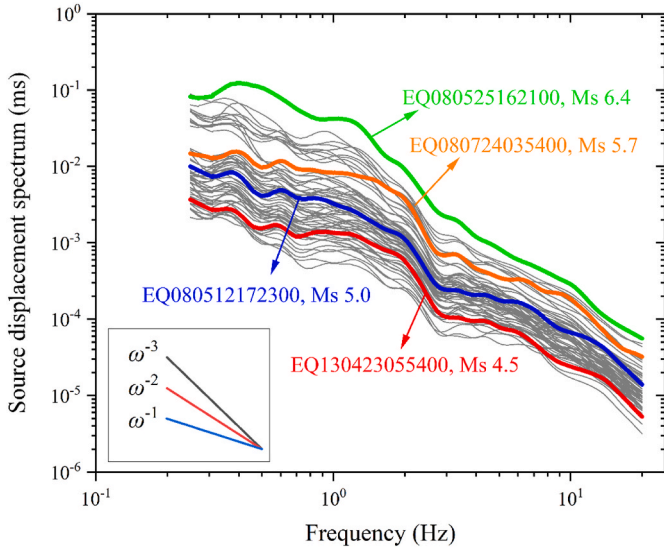


**Fig. 7.** The inverted source displacement spectrum for 62 selected earthquake events (gray lines). The green (Ms 6.4), orange (Ms 5.7), blue (Ms 5.0) and red (Ms 4.5) solid lines represent typical events with four magnitudes. The name of the earthquake event consists of the date and time when the earthquake occurred.

repeated processes were adopted. The source component that follows Brune's  $\omega^2$  model of the  $i$ th earthquake event obtained from the GIT can be written as follows [26,46]:

$$S_i(f) = \frac{R_{\theta p} V F}{4\pi\rho_s\beta^3 R_0} \times \frac{(2\pi f)^2 M_{0i}}{1 + (f/f_{0i})^2} \quad (9)$$

where  $R_{\theta p} = 0.55$ ,  $V = 0.707$ ,  $F = 2$ ,  $\beta = 3.6$  km/s, and  $\rho_s = 2.7$  g/cm<sup>3</sup> represent the radiation pattern coefficient, the proportion of shear-wave energy in the horizontal component, the free surface amplification, shear-wave velocity and density near the source, respectively.  $R_0 = 1$  km denotes the reference distance [26].  $M_{0i}$  and  $f_{0i}$  denote the seismic moment and corner frequency of the  $i$ th earthquake, respectively.

In our scheme, the relation between moment magnitude  $M_w$  and seismic moment was adopted as follows [46]:

$$M_w = \frac{2}{3} \log M_0 - 10.7 \quad (10)$$

The moment rate spectrum can be defined by [7].

$$\dot{M}_{0i}(f) = \frac{M_{0i}}{1 + (f/f_{0i})^2} \quad (11)$$

The fitting variance was used to determine the source parameters [47]:

$$RMS_i(M_0, f_0, \kappa_0) = \sqrt{\frac{\sum_j^N \{ \log[\dot{M}_{0i}^j(f_j)] - \log[\dot{M}_{0i}^T(f_j)] \}^2}{N}} \quad (12)$$

where  $\dot{M}_{0i}^j(f_j)$  and  $\dot{M}_{0i}^T(f_j)$  denote the inverted and theoretical moment rate spectrum of the  $i$ th event at the  $j$ th frequency, respectively.  $N$  denotes the number of frequencies.

A grid-searching approach was performed to estimate the best-fitting seismic moment  $M_0$  and corner frequency  $f_0$  for individual events to minimize the fitting variance defined by Equation (12). By considering a range of  $M_s - 1.0 \leq M \leq M_s + 1.0$ , the stress parameters for small and medium-sized earthquake events range from 1 to 1000.0 bars [48]. Then, the corner frequency is defined as  $f_0 = 4.9 \times 10^6 \beta (\Delta\sigma/M_0)^{1/3}$  based on Brune's model. The slope of the best-fit source displacement spectrum in Fig. 7 indicates that the calculated source spectrum

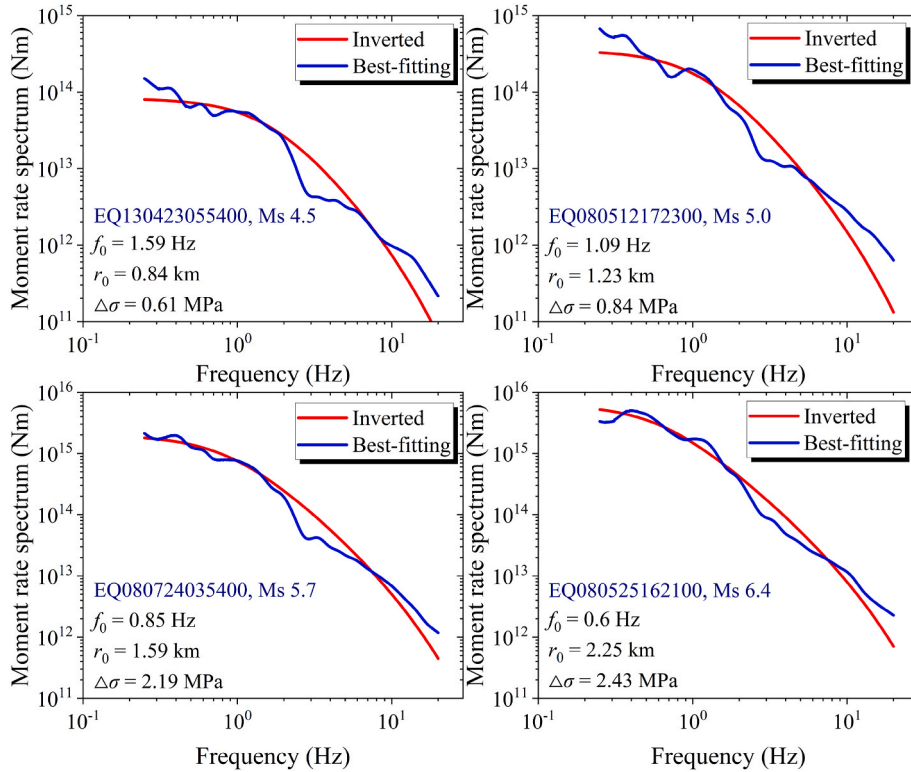


**Fig. 8.** The best-fitting (blue) and inverted (red) moment rate spectra for four typical earthquake events with different magnitudes. The source parameters, such as corner frequency  $f_0$ , source radius  $r$ , and stress drop  $\Delta\sigma$ , obtained in this study are also shown in each panel. The red solid line indicates the inverted model from 50 bootstrap inversions.

**Table 2**

Magnitude  $M$ , corner frequency  $f_0$ , moment magnitude  $M_w$ , seismic moment  $M_0$ , radius  $r$ , stress parameter  $\Delta\sigma$  and radiated energy  $E_s$  obtained from GIT for each event selected in this study.

No.	Event ID	Lat.	Long.	M	$f_0$	$M_w$	$M_0$	$r$	$\Delta\sigma$	Es
1	EQ080512144300	31.27	103.82	6.3	0.85	4.67	1.12E+16	1.59	1.23	1.52E+11
2	EQ080512191100	31.26	103.67	6.3	0.60	4.92	2.66E+16	2.25	1.03	3.12E+11
3	EQ080512214000	31.02	103.65	5.2	0.60	4.58	8.41E+15	2.25	0.32	3.12E+10
4	EQ080513040800	31.43	104.06	5.8	0.85	4.83	2.00E+16	1.59	2.19	4.84E+11
5	EQ080513074600	31.34	103.58	5.4	1.09	4.33	3.55E+15	1.23	0.84	3.10E+10
6	EQ080512145400	31.26	103.59	5.8	0.60	4.67	1.12E+16	2.25	0.43	5.54E+10
7	EQ080512153400	31.29	103.77	5.8	1.09	4.25	2.66E+15	1.23	0.63	1.74E+10
8	EQ080513150700	30.95	103.42	6.1	0.60	4.83	2.00E+16	2.25	0.77	1.77E+11
9	EQ080512150100	31.45	104.49	5.5	1.59	4.42	4.73E+15	0.84	3.45	1.57E+11
10	EQ080512162100	31.53	104.28	5.5	1.59	4.25	2.66E+15	0.84	1.94	4.97E+10
11	EQ080512170600	31.16	103.69	5.2	1.84	4.00	1.12E+15	0.73	1.27	1.31E+10
12	EQ080512173100	31.16	103.56	5.2	1.34	4.17	2.00E+15	1.00	0.87	1.75E+10
13	EQ080512174200	31.48	104.13	5.3	1.09	4.42	4.73E+15	1.23	1.12	5.50E+10
14	EQ080512162600	31.40	104.12	5.1	2.34	4.00	1.12E+15	0.57	2.59	2.48E+10
15	EQ080512201300	31.39	103.63	4.3	2.83	3.75	4.73E+14	0.47	1.95	7.24E+09
16	EQ080512221000	31.34	103.59	4.6	2.34	3.75	4.73E+14	0.57	1.09	4.43E+09
17	EQ080512230500	31.05	103.42	5.1	1.34	4.25	2.66E+15	1.00	1.17	3.10E+10
18	EQ080513010300	31.10	103.65	4.6	1.84	4.08	1.50E+15	0.73	1.69	2.35E+10
19	EQ080513012900	31.21	103.68	4.9	2.09	4.00	1.12E+15	0.64	1.85	1.84E+10
20	EQ080513015400	31.26	103.62	5.1	1.34	4.25	2.66E+15	1.00	1.17	3.10E+10
21	EQ080513044500	31.73	104.55	5.2	0.85	4.42	4.73E+15	1.59	0.52	2.71E+10
22	EQ080513101500	31.58	104.11	4.3	2.34	3.75	4.73E+14	0.57	1.09	4.43E+09
23	EQ080513103300	31.27	103.81	4.3	4.07	3.58	2.66E+14	0.33	3.26	5.60E+09
24	EQ080513162000	31.36	104.05	4.8	1.59	4.17	2.00E+15	0.84	1.46	2.81E+10
25	EQ080514105400	31.34	103.63	5.8	0.60	4.67	1.12E+16	2.25	0.43	5.54E+10
26	EQ080514172600	31.41	104.12	5.1	1.34	4.33	3.55E+15	1.00	1.56	5.52E+10
27	EQ080513075400	31.28	103.63	5.2	1.34	4.25	2.66E+15	1.00	1.17	3.10E+10
28	EQ080516132500	31.31	103.45	5.9	0.85	4.75	1.50E+16	1.59	1.64	2.72E+11
29	EQ080512161000	31.14	103.60	5.5	1.34	4.17	2.00E+15	1.00	0.87	1.75E+10
30	EQ080512201500	31.87	104.57	4.9	1.34	4.08	1.50E+15	1.00	0.66	9.86E+09
31	EQ080514095600	31.19	103.80	4.4	2.58	3.83	6.31E+14	0.52	1.97	1.02E+10
32	EQ080514135400	31.95	104.24	4.7	1.34	4.25	2.66E+15	1.00	1.17	3.10E+10
33	EQ080513155300	32.24	105.10	4.7	1.59	4.08	1.50E+15	0.84	1.09	1.58E+10
34	EQ080512172300	32.19	104.92	5.0	1.84	3.92	8.41E+14	0.73	0.95	7.39E+09
35	EQ080512194100	32.22	105.09	4.8	2.58	3.67	3.55E+14	0.52	1.11	3.22E+09
36	EQ080512221500	32.12	104.77	4.6	1.84	3.92	8.41E+14	0.73	0.95	7.39E+09
37	EQ080513015200	31.82	104.58	4.7	1.84	4.00	1.12E+15	0.73	1.27	1.31E+10
38	EQ080513045100	32.33	105.17	4.7	1.84	4.00	1.12E+15	0.73	1.27	1.31E+10
39	EQ080513151900	32.35	105.24	5.1	1.59	4.17	2.00E+15	0.84	1.46	2.81E+10
40	EQ080512224600	32.72	105.64	5.1	1.34	4.33	3.55E+15	1.00	1.56	5.52E+10
41	EQ080518010800	32.20	105.08	6.1	0.85	4.83	2.00E+16	1.59	2.19	4.84E+11
42	EQ080525162100	32.55	105.48	6.4	0.60	5.17	6.31E+16	2.25	2.43	1.76E+12
43	EQ080724150900	32.76	105.61	6.0	0.60	4.92	2.66E+16	2.25	1.03	3.12E+11
44	EQ080527163700	32.78	105.70	5.7	1.09	4.67	1.12E+16	1.23	2.66	3.08E+11
45	EQ080724035400	32.72	105.63	5.7	0.35	5.08	4.73E+16	3.85	0.36	1.99E+11
46	EQ130420080600	30.20	102.90	4.8	0.85	4.33	3.55E+15	1.59	0.39	1.53E+10
47	EQ130420113400	30.10	102.90	5.3	0.85	4.50	6.31E+15	1.59	0.69	4.82E+10
48	EQ130420103800	30.20	102.90	4.6	1.09	4.08	1.50E+15	1.23	0.35	5.53E+09
49	EQ130420093900	30.10	102.90	4.5	1.09	4.00	1.12E+15	1.23	0.27	3.08E+09
50	EQ130420191200	30.30	103.00	4.5	1.84	3.83	6.31E+14	0.73	0.71	4.16E+09
51	EQ130420092600	30.20	102.90	4.4	1.59	3.83	6.31E+14	0.84	0.46	2.80E+09
52	EQ130420092000	30.20	102.90	4.6	1.34	4.08	1.50E+15	1.00	0.66	9.86E+09
53	EQ130420080700	30.30	102.90	5.1	0.85	4.42	4.73E+15	1.59	0.52	2.71E+10
54	EQ130420101900	30.30	102.90	4.3	2.09	3.83	6.31E+14	0.64	1.04	5.85E+09
55	EQ130421221600	30.30	102.90	4.3	1.59	3.92	8.41E+14	0.84	0.61	4.97E+09
56	EQ130420093700	30.30	102.90	4.9	1.34	4.17	2.00E+15	1.00	0.87	1.75E+10
57	EQ130420090200	30.30	102.90	4.6	1.84	3.92	8.41E+14	0.73	0.95	7.39E+09
58	EQ130421170500	30.30	103.00	5.4	0.85	4.42	4.73E+15	1.59	0.52	2.71E+10
59	EQ130423055400	30.40	103.00	4.5	1.59	3.92	8.41E+14	0.84	0.61	4.97E+09
60	EQ130420091100	30.20	102.80	4.3	1.59	4.08	1.50E+15	0.84	1.09	1.58E+10
61	EQ130421045300	30.30	103.00	5.0	1.59	4.17	2.00E+15	0.84	1.46	2.81E+10
62	EQ130421115900	30.20	103.00	4.9	1.09	4.25	2.66E+15	1.23	0.63	1.74E+10

Unit: Lat., °; Long., °;  $f_0$ , Hz;  $M_0$ , (Nm);  $r$ , km;  $\Delta\sigma$ , MPa; Es, J.

The event ID can be divided into data and time of this earthquake. For example, EQ130420101900 indicates that the earthquake occurred on April 20, 2013 at 10:19:00 (Local time).

basically conforms to Brune’s source model. Fig. 8 displays the derived source parameters of four typical earthquake events (Ms 4.5, 5.0, 5.7 and 6.4). The detailed inversion results are summarized in Table 2.

Based on the derived source parameters, the relationship between the seismic moment and corner frequency can be written as follows:

$$\log M_0 = (22.68 \pm 0.06) - (2.43 \pm 0.29)\log f_0 \quad (13)$$

The relation shows that the corner frequency decreases with increasing seismic moment, and the rate on a logarithmic scale is 2.43, which is in agreement with the results given by Dutta et al. [49]. However, self-similarity in the seismic source indicates that the product

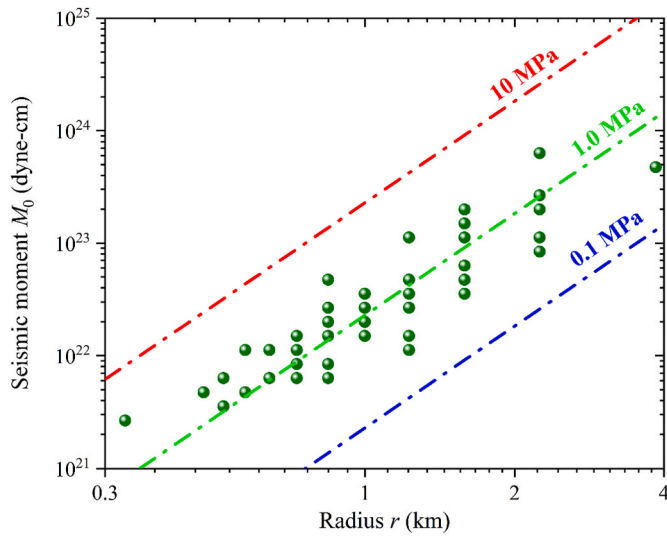


**Fig. 9.** The moment magnitude  $M_0$  versus source radius  $r$ . The balls indicate the event used in this study. The red, green and blue dotted-dashed lines indicate the constant stress parameter relationships corresponding to 10, 1.0, and 0.1 MPa, respectively.

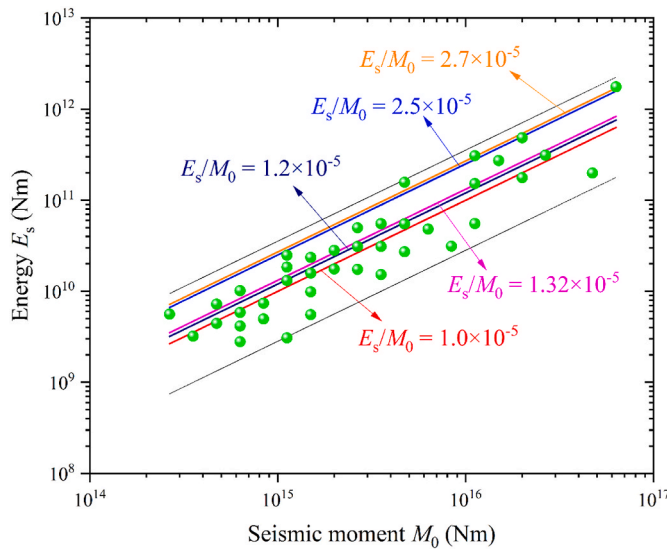


**Fig. 10.** The radiated energy  $E_s$  versus seismic moment  $M_0$ . Solid lines in red, orange, dark blue, blue, and magenta represent the inversion results obtained from this study ( $E_s/M_0 = 1.0 \times 10^{-5}$ ), Wantanabe et al. [50] ( $E_s/M_0 = 2.7 \times 10^{-5}$ ), Dutta et al. [51] ( $E_s/M_0 = 1.2 \times 10^{-5}$ ), Hassani et al. [7] ( $E_s/M_0 = 2.5 \times 10^{-5}$ ), and Wang et al. [15] ( $E_s/M_0 = 1.32 \times 10^{-5}$ ), respectively. The light solid lines indicate the range of the average plus or minus one standard deviation.

of  $M_0$  and  $f_c^\beta$  should be a constant related to the stress parameter. Therefore, fixing the slope of Equation (13) to  $-3$ , we can obtain the following relation:

$$\log M_0 = (22.75 \pm 0.07) - 3 \log f_0 \quad (14)$$

In addition, the corner frequencies are between 0.3 and 4.1 Hz, and the source radii are between 0.3 and 4 km, which agree best with the inversion results given by Wang et al. [15], indicating that the corner frequencies for the Wenchuan aftershocks with  $M_s$  3.2–6.5 range from 0.1 to 3.1 Hz. The corner frequency values in our model are also well matched with the results given by Hassani et al. [7] inverted for earthquake events with  $M$  3.5–7.3 in central and eastern Iran.

The widely used earthquake source model is defined as the  $\omega^2$  model

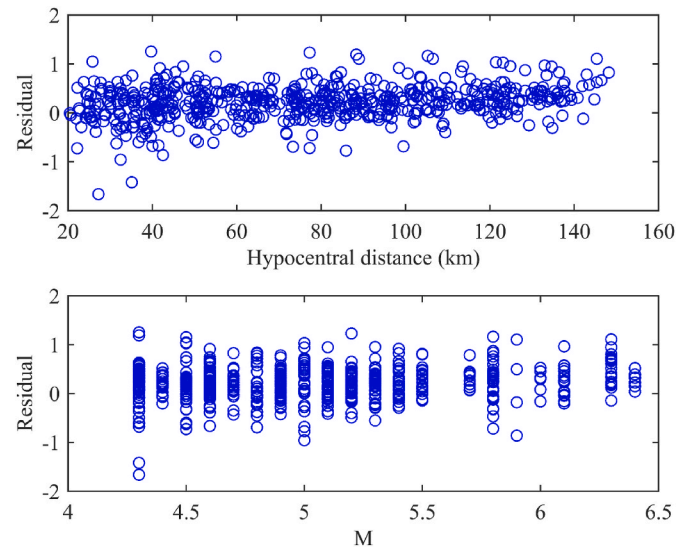


**Fig. 11.** Residual of the Fourier amplitude spectrum versus hypocentral distance (upper) and magnitude  $M$  (bottom).

[46]. Based on this model, the source radius  $r$  and the stress parameter  $\Delta\sigma$  for each earthquake event can be obtained as follows:

$$r_i = \frac{2.34\beta}{2\pi f_{0i}} \quad (15)$$

$$\Delta\sigma_i = \frac{7M_{0i}}{16r_i^3} \times 10^{-21} \quad (16)$$

where  $r_i$  denotes the source radius in km, and  $\Delta\sigma_i$  indicates the stress drop in bars. The remaining parameters, such as  $\beta$  and  $M_{0i}$  are in units of km/s and dyne. cm, respectively. The relation between the seismic moment  $M_0$  and source radius  $r$  is plotted in Fig. 9, indicating that the stress calculated in this study is between 0.2 MPa and 3.5 MPa with an average value of 1.2 MPa, which is well matched with the results inverted by Zhou et al. [9].

The radiated shear-wave energy for individual earthquake events in the frequency band ranging from 0.25 to 20 Hz was obtained using the following relationship [50]:

$$E_s = \left[ \frac{1}{15\pi\rho_s\alpha_s^3} + \frac{1}{10\pi\rho_s\beta^5} \right] \int_{-\infty}^{+\infty} \left[ 2\pi f \frac{M_0}{1 + (f/f_c)^2} \right]^2 df \quad (17)$$

where  $\alpha$  denotes the P-wave velocity near the earthquake source and can be set as 6.1 km/s [15]. The relationship between the shear-wave energy ( $E_s$ ) and seismic moment ( $M_0$ ) was obtained as follows:

$$\log(E_s) = (-5 \pm 0.06) + \log(M_0) \quad (18)$$

A comparison between the inversion results obtained from this study and other studies is plotted in Fig. 10. Solid lines in red, orange, dark blue, blue, and magenta represent the inversion results obtained from this study, Wantanabe et al. [51], Dutta et al. [52], Hassani et al. [7], and Wang et al. [15]. The energy-to-moment ratio  $E_s/M_0 = 1.0 \times 10^{-5}$  in the frequency range of 0.25–20 Hz defined by Equation (18) is well matched with the inversion model  $E_s/M_0 = 1.32 \times 10^{-5}$  for the after-shock sequence of the 2008 Wenchuan, China, earthquake in the frequency range of 0.1–20 Hz given by Wang et al. [15] and  $E_s/M_0 = 1.2 \times 10^{-5}$  for weak-motion records in Anchorage, Alaska area in the frequency range of 0.2–20 Hz given by Dutta et al. [52], while lower than the model  $E_s/M_0 = 2.5 \times 10^{-5}$  for earthquakes in the east-central Iran in the frequency range of 0.4–15 Hz given by Hassani et al. [7] and  $E_s/M_0 = 2.7 \times 10^{-5}$  for small and medium-sized earthquake events in the Kanto, Japan region in the frequency range of 0.05–32 Hz given by

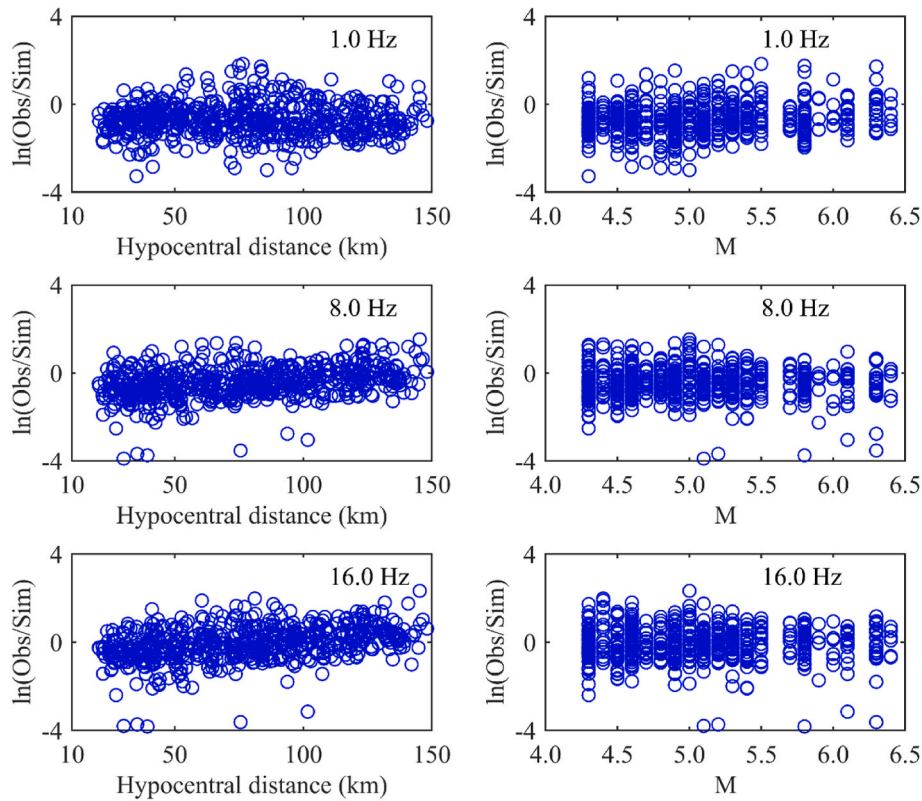


**Fig. 12.** Residual of the Fourier amplitude spectrum at frequency points of 1.0, 8.0, and 16.0 Hz, defined as a function of hypocentral distance  $R$  (left panel) and magnitude  $M$  (right panel).

Watanabe et al. [51]. This difference may be caused by the limited frequency range of the spectral data used in the inversion [7].

### 5.5. Inversion residual

In this study, a residual defined as a function of hypocentral distance  $R_{\text{hyp}}$  and magnitude  $M$  was used to investigate whether there was any bias in the inversion results. The residuals are determined as the difference between the natural log ( $\ln$ ) of the recorded FAS and the natural log ( $\ln$ ) of the estimated FAS. The relations between residuals and hypocentral distance and magnitude are plotted in Figs. 11 and 12. The residual indicates no significant differences when  $R_{\text{hyp}} < 100$  km and the magnitude is lower than 6.0. The residual in each panel falls near zero-reference line and there is no remarkable trend with respect to distance and magnitude in the bias, especially at lower frequencies, which is well matched with the results given by previous studies [7,53]. However, when the distances are greater than 100 km, there is a significant bias. This may be resulted from the contribution of Moho interface reflected waves to the overall seismic recorded energy or the inappropriate geometric spreading model. Besides, the underestimation of the simulated FAS with magnitudes above 6.0 may be due to inappropriate source models. In fact, it is well known that Brune's source model with a single corner frequency is usually adopted to describe the small to moderate earthquakes [7,54,55].

## 6. Discussion and conclusion

In this study, a generalized inversion technique was applied to the recordings recorded by 55 strong-motion stations during 62 earthquake events of  $M_s$  4.3–6.4 that occurred in the Longmenshan and Aninghe fault zones. The source, path and site components can be separated in the GIT approach, and then these parameters related to the source, path and site, such as seismic moment, corner frequency, stress parameter,

quality factor and site effect, can be estimated easily to help the study of seismic disasters and risk assessment in the study area.

According to the strong motion data recorded by stations in western-central Sichuan with hypocentral distances between 20 km and 150 km and peak ground accelerations between 2  $\text{cm/s}^2$  and 100  $\text{cm/s}^2$ . The quality factor  $Q(f)$  in this area is regressed as  $Q(f) = 219.4f^{0.7383}$ , indicating that the energy absorption of seismic waves in the near-field region is slow. Our  $Q(f)$  model agrees best with the simulation results of the model  $Q(f) = 217.8f^{0.816}$  given by Zhang et al. [30] for the Sichuan Basin region. However, the fitting results are very similar to the model  $Q(f) = 334.4f^{0.581}$  given by Qiao et al. [31] in the 10–20 Hz frequency band but smaller than those models of Zhang et al. [30] and Qiao et al. [31] in other frequency bands. Moreover, our fitting results are greater than the results of Wang et al. [15] and Fu et al. [24] in the frequency range less than 3 Hz, while in the frequency range greater than 3 Hz, they are less than the results given by Wang et al. [15] and Fu et al. [24]. However, the result given by Li et al. [25] for Changning earthquake are quite different from others, especially in the high frequencies with  $f$  greater than 4 Hz.

The comparison of the inversion results of the site effect at 55 strong-motion stations indicates that the predominant frequency peaks estimated by the GIT and H/V approaches are well matched with each other. Nevertheless, the site amplification factor calculated by the GIT is greater than that calculated by the H/V method, especially in the frequency band near the predominant frequency.

In the seismic moment range between  $10^{22}$  and  $10^{27}$  dyne cm, we obtained the relationship  $M_0 f_0^3 = 5.6 \times 10^{23}$  dyne  $\text{cm/s}^3$ , in which  $M_0$  and  $f_0$  indicate the seismic moment and corner frequency, respectively. In addition, the stress parameter values obtained for each earthquake event are between 0.2 MPa and 3.5 MPa with an average value of 1.2 MPa. The results are well matched with the results inverted by Zhou et al. [9], who argue that the stress drop values for the Yangbi earthquake are between 0.1 and 2.7 MPa. Moreover, the stress parameter

values given in this study are also well matched with the results of the Wenchuan earthquake [15] and agree with shallow crustal earthquakes all over the world [15,56–58]. The corner frequencies are between 0.3 and 4.1 Hz, and the source radii are between 0.3 and 4 km, which agree best with the inversion results given by Wang et al. [15].

Finally, a residual defined as a function of hypocentral distance ( $R$ ) and moment magnitude ( $M_0$ ) was used to investigate whether there was any bias in the inversion results. The residual analysis results indicate that the geometric spreading model and single corner frequency source model used in this study resulted in an underestimation of the Fourier amplitude level in the far field and for large earthquakes.

## Funding

This research was supported by the National Natural Science Foundation for Young Scientists of China (Grant No. 42204050), the National Natural Science Foundation of China (No. U2139203), the Hong Kong Research Grant Council Grants (Nos. 14303721 and 14306122), Faculty of Science in The Chinese University of Hong Kong, the National Key Research and Development Program of China (Grant No. 2022YFC3003601), the Postdoctoral Program of International Training Program for Young Talents of Guangdong Province, and the Postdoctoral Office of Guangzhou City, China (Grant No. 62216242).

## Author statement

Pengfei Dang: Conceptualization, Methodology, Software, Data curation, Resources, Formal analysis, Validation, Visualization, Investigation, Supervision, Writing—original draft, Writing—review & editing, Project administration. Jie Cui: Supervision, Project administration. Hongfeng Yang: Project administration, Supervision. Jian Song: Methodology, Software, Data curation.

## Declaration of competing interest

The author(s) declared no potential conflicts of interest with respect to the research, authorship, and/or publication of this article.

## Data availability

The authors do not have permission to share data.

## Acknowledgements

The authors thank the China Strong Ground Motion Networks Center for providing the recordings used in this study. The authors sincerely thank American Journal Experts (<https://www.aje.com>) for providing the linguistic assistance during the preparation of the original manuscript. In addition, the authors would like to show their thanks to two anonymous reviewers, the Editor-in-Chief, and the editors related for their valuable comments and suggestions that improved the article.

## References

- Cultrera G, Luzi L, Ameri G, Augliera P, Azzara R, Bergamaschi F, Bertrand E, Bordoni P, Cara F, Cogliano R, Alema ED, Giacomo DD, Giulio GD, Duval A, Fodarella A, Franceschina G, Gallipoli MR, Harabaglia, Ladina C, Lovati S, Marzorati S, Massa M, Milana G, Mucciarelli M, Pacor F, Parolai S, Picozzi M, Puglia R, Pucillo S, Régnier J, Riccio G, Salichon J, Sobiesiak M. Evaluation of the local site effects in the upper and middle Aterno valley, Numero speciale Abruzzo. Seismic Action and site effects. Progettazione sismica 2009; 03. IUSS Press; 2009.
- Andrews DJ. Objective determination of source parameters and similarity of earthquakes of different size. *Geophys Monogr* 1986;37:259–67.
- Castro RR, Anderson JG, Singh SK. Site responses, attenuation, and source spectra of S wave along the Guerrero, Mexico subduction zone. *Bull Seismol Soc Am* 1990; 80(6A):1481–503.
- Oth A, Bindi D, Parolai S. Earthquake scaling characteristics and the scale-(in) dependence of seismic energy-to-moment ratio: insights from KiK-net data in Japan. *Geophys Res Lett* 2010;37(19):470–9.
- Ameri G, Oth A, Pilz M, Bindi D, Parolai S, Luzi L, Mucciarelli M, Cultrera G. Separation of source and site effects by generalized inversion technique using the aftershock recordings of the 2009 L'Aquila earthquake. *Bull Earthq Eng* 2011;9(3): 717–39.
- Mandal P, Dutta U. Estimation of earthquake source parameters in the Kachchh seismic zone, Gujarat, India, from strong-motion network data using a generalized inversion technique. *Bull Seismol Soc Am* 2011;101(4):1719–31.
- Hassani B, Zafarani H, Farjoodi J, Ansari A. Estimation of site amplification, attenuation and source spectra of S-waves in the East-Central Iran. *Soil Dynam Earthq Eng* 2011;31(10):1397–413.
- Jeong S, Stump BW, Deshon HR. Spectral characteristics of ground motion from induced earthquakes in the Fort Worth Basin, Texas, using the generalized inversion technique. *Bull Seismol Soc Am* 2020;110(5):2058–76.
- Zhou Y, Wang HW, Wen RZ, Miao TM, Cui JW. Source characteristics and path attenuation for the Yangbi, China seismic sequence in 2021. *Pure Appl Geophys* 2022;179(8):2721–33.
- Guo Z, Guan M, Chapman MC. Amplification and attenuation due to geologic conditions in the Sichuan Basin, Central China. *Seismol Res Lett* 2023;94(1): 399–413.
- Ren YF, Wen RZ, Yamanaka H, Kasima T. Site effects by generalized inversion technique using strong motion recordings of the 2008 Wenchuan earthquake. *Earthq Eng Vib* 2013;12(2):165–84.
- Wu WW, Su JR, Wei YL, Wu P, Li J, Sun W. Discussion on attenuation characteristics, site responses and magnitude determination in Sichuan. *Seismol Geol* 2016;38(4):1005–18 (in Chinese).
- Song J, Shi LJ, Dang PF, Tan JY. Study on site amplification of strong ground motion stations considering attenuation characteristics of the sea area in the Sagami Bay area. *Japan. China Civil Engineering Journal* 2021;54:74–84 (in Chinese).
- Ren YF. Study on site effect in the Wenchuan earthquake. Harbin: Institute of Engineering Mechanics, China Earthquake Administration; 2014 (in Chinese).
- Wang HW, Ren YF, Wen RZ. Source parameters, path attenuation and site effects from strong-motion recordings of the Wenchuan aftershocks (2008–2013) using a non-parametric generalized inversion technique. *Geophys J Int* 2018;212(2): 872–90.
- Husid P. Gravity effects on the earthquake response of yielding structures. In: Report of earthquake engineering research. Laboratory Pasadena, California Institute of Technology; 1967.
- McCann MWJ. Determining strong motion duration of earthquakes. *Bull Seismol Soc Am* 1979;69(4):1253–65.
- Pacor F, Spallarossa D, Oth A. Spectral models for ground motion prediction in the L'Aquila region (central Italy): evidence for stress-drop dependence on magnitude and depth. *Geophys J Int* 2016;204(2):697–718.
- Konno K, Ohmachi T. Ground-motion characteristics estimated from ratio between horizontal and vertical components of microtremor. *Bull Seismol Soc Am* 1998;88 (1):228–41.
- Dang PF, Cui J, Liu QF. Parameter estimation for predicting near-field strong ground motion and its application to Lushan earthquake in China. *Soil Dynam Earthq Eng* 2022;156:107223.
- Dang PF, Cui J, Liu QF, Li YD. Simulation of earthquake ground motion via stochastic finite-fault modeling considering the effect of rupture velocity. *Stoch Environ Res Risk Assess* 2023;37(6):2225–41.
- Atkinson GM, Mereu RF. The shape of ground motion attenuation curves in southeastern Canada. *Bull Seismol Soc Am* 1992;82(5):2014–31.
- Dang PF, Liu QF. Stochastic finite-fault ground motion simulation for the Mw 6.7 earthquake in Lushan, China. *Nat Hazards* 2020;100(3):1215–41.
- Fu L, Li XJ, Wang F, Su C. A study of site response and regional attenuation in the Longmen Shan region, eastern Tibetan plateau, SW China, from seismic recordings using the generalized inversion method. *J Asian Earth Sci* 2019;181:103887.
- Li J, Zhou B, Rong M, Chen S, Zhou Y. Estimation of source spectra, attenuation, and site responses from strong-motion data recorded in the 2019 Changning earthquake sequence. *Bull Seismol Soc Am* 2020;110(2):410–26.
- Boore DM. Simulation of ground motion using the stochastic method. *Pure Appl Geophys* 2003;160(3):635–76.
- Atkinson GM, Hough SE. A model for the shape of the Fourier amplitude spectrum of acceleration at high frequencies. *Bull Seismol Soc Am* 1984;86(1):106–12.
- Menke W. Geophysical data analysis: discrete inverse theory. In: Dmowska R, Holton JR, editors. *Int geophysical series*, vol. 45. Academic Press; 1989. p. 289.
- Askan A, Sisman FN, Pekcan O. A regional near-surface high frequency spectral attenuation ( $\kappa$ ) model for northwestern Turkey. *Soil Dynam Earthq Eng* 2014; 65:113–25.
- Zhang YJ, Qiao HZ, Cheng WZ, Liu J. Attenuation characteristic of the media in Sichuan Basin region. *J Seismol Res* 2007;30(1):43–8 (in Chinese).
- Qiao HZ, Zhang YJ, Cheng WZ, Liu J. The inversion of the inelastic coefficient of the medium in North-West of Sichuan province. *Seismological and Geomagnetic Observation and Research* 2006;27(4):1–7 (in Chinese).
- Wang HW, Ren YF, Wen RZ. Research progress of generalized inversion technique used for separating source, path and site effect from ground motions. *Prog Geophys* 2017;32(1):78–86 (in Chinese).
- Wen RZ, Wang HW, Ren YF, Kun Ji. Estimation of source parameters and quality factor based on generalized inversion method in Lushan earthquake. *J Harbin Inst Technol* 2015;47(4):58–63.
- Lermo J, Chavez-Garcia F. Site effect evaluation using spectral ratios with only one station. *Bull Seismol Soc Am* 1993;83(5):1574–94.
- Parolai S, Richwalski SM. The importance of converted waves in comparing H/V and RSM site response estimate. *Bull Seismol Soc Am* 2004;94(1):304–13.

- [36] Field H, Jacob K. Comparison of various site response estimation techniques, including three that are not reference site dependent. *Bull Seismol Soc Am* 1995;85(4):1127–43.
- [37] Theodulidis N, Bard PY. Horizontal to vertical spectral ratio and geological conditions: an analysis of strong motion data from Greece and Taiwan (SMART-1). *Soil Dynam Earthq Eng* 1995;14(3):177–97.
- [38] Bonilla LF, Steidl JH, Lindley GT, Tumarkin AG, Archuleta RJ. Site amplification in the San Fernando valley, California: variability of site-effect estimation using the S-wave, coda and H/V methods. *Bull Seismol Soc Am* 1997;87(3):710–30.
- [39] Sokolov VY, Loh CH, Jean WY. Application of horizontal-to-vertical (H/V) Fourier spectral ratio for analysis of site effect on rock (NEHRP-class B) sites in Taiwan. *Soil Dynam Earthq Eng* 2007;27(4):314–23.
- [40] Bard PY. Microtremor measurements: a tool for site effect estimation? In proceedings of the 2nd international symposium on effects of surface geology on seismic motion. Yokohama, Japan 1998;3:1251–82.
- [41] Castro RR, Rovelli A, Cocco M, Bona MD, Pacor F. Stochastic simulation of strong-motion records from the 26 September 1997 (Mw 6) Umbria-Marche (Central Italy) earthquake. *Bull Seismol Soc Am* 2001;91(1):27–39.
- [42] Castro RR, Pacor F, Bindi D, Franceschina G, Luzi L. Site response of strong motion stations in the Umbria, Central Italy, region. *Bull Seismol Soc Am* 2004;94(2):576–90.
- [43] Salazar W, Sardina V, Cortina JDA. A hybrid inversion technique for the evaluation of source, path, and site effects employing S-wave spectra for subduction and upper-crustal earthquakes in El Salvador. *Bull Seismol Soc Am* 2007;97(1B):208–21.
- [44] Ameri G, Oth A, Polz M, Bindi D, Parolai S, Luzi L, Mucciarelli M, Cultrera G. Separation of source and site effects by generalized inversion technique using the aftershock recordings of the 2009 L'Aquila earthquake. *Bull Earthq Eng* 2011;9:717–39.
- [45] Oth A, Bindi D, Parolai S, Giacomo DD. Spectral analysis of K-NET and KiK-net data in Japan, Part II: on attenuation characteristics, source spectra, and site responses of borehole and surface stations. *Bull Seismol Soc Am* 2011;101:667–87.
- [46] Brune JN. Tectonic stress and the spectra of seismic shear waves from earthquakes. *J Geophys Res* 1970;75(26):4997–5009.
- [47] Hanks TC, Kanamori H. A moment magnitude scale. *J Geophys Res* 1979;84(B5):2348–50.
- [48] Kanamori H. Mechanics of earthquake. *Annu Rev Earth Planet Sci* 1994;22:207–37.
- [49] Dutta U, Martirosyan A, Biswas N, Papageorgiou A, Combellick R. Estimation of S-wave site response in Anchorage, Alaska, from weak-motion data using generalized inversion method. *Bull Seismol Soc Am* 2001;91(2):335–246.
- [50] Vassiliou MS, Kanamori H. The energy release in earthquakes. *Bull Seismol Soc Am* 1982;72(2):371–87.
- [51] Watanabe K, Sato H, Kinoshita S, Ohtake M. Source characteristics of small to moderate earthquakes in the Kanto region, Japan: application of a new definition of the S-wave time window length. *Bull Seismol Soc Am* 1996;86(5):1284–91.
- [52] Dutta U, Biswas N, Martirosyan A, Papageorgiou A, Kinoshita S. Estimation of earthquake source parameters and site responses in Anchorage, Alaska from strong-motion network data using generalized inversion method. *Phys Earth Planet In* 2003;137:13–29.
- [53] Sadeghi-Bagherabadi A, Sobouti F, Pachhai S, Aoudia A. Estimation of geometrical spreading, quality factor and kappa in the Zagros region. *Soil Dynam Earthq Eng* 2020;133:106110.
- [54] Boatwright J, Choy GL. Acceleration source spectra anticipated for large earthquakes in northeastern North America. *Bull Seismol Soc Am* 1992;82(2):660–82.
- [55] Atkinson GM, Boore DM. Ground-motion relations for eastern north America. *Bull Seismol Soc Am* 1995;85(1):17–30.
- [56] Trugman DT, Shearer PM. Application of an improved spectral decomposition method to examine earthquake source scaling in southern California. *J Geophys Res Solid Earth* 2017;122(4):2890–910.
- [57] Baltay AS, Hanks TC, Abrahamson NA. Earthquake stress drop and Arias intensity. *J Geophys Res Solid Earth* 2019;124(4):3838–52.
- [58] Wang HW, Ren YF, Wen RZ. Breakdown of earthquake self-similar scaling and source rupture directivity in the 2016-2017 Central Italy seismic sequence. *J Geophys Res Solid Earth* 2019;124(4):3898–917.